Wavefunction engineering of layered semiconductors: theoretical foundations

2006 J. Phys.: Condens. Matter 18 R901

(http://iopscience.iop.org/0953-8984/18/49/R01)

INSTITUTE OF PHYSICS PUBLISHING JOURNAL OF PHYSICS: CONDENSED MATTER

J. Phys.: Condens. Matter **18** (2006) R901–R917 doi:10.1088/0953-8984/18/49/R01

TOPICAL REVIEW

Wavefunction engineering of layered semiconductors: theoretical foundations

L R Ram-Mohan[1] **and K H Yoo**[1,2]

[1] Departments of Physics, Electrical and Computer Engineering, Worcester Polytechnic Institute, Worcester, MA 01609, USA
[2] Department of Physics and Research Institute for Basic Sciences, Kyung Hee University, Seoul 130-701, Korea

E-mail: lrram@wpi.edu

Received 8 November 2006
Published 22 November 2006
Online at stacks.iop.org/JPhysCM/18/R901

Abstract

We present the theoretical basis of wavefunction engineering. We show that a Lagrangian formulation for the valence bands of bulk semiconductors in the $\mathbf{k} \cdot \mathbf{P}$ model provides a direct approach to determining derivative operator ordering in the multiband description of electronic states in semiconductors in the envelope function approximation. The current continuity condition is also obtained through a gauge variation on the Lagrangian. This naturally leads into a finite element approach for the discretization of Schrödinger's equation. Furthermore, by including the Poisson Lagrangian a self-consistent treatment of the Schrödinger–Poisson band-bending in arbitrarily doped structures can be calculated. The theory is developed for both the zinc blende and wurtzite structured compound semiconductors and their heterostructures. Calculations for quantum wells and superlattices are presented to illustrate wavefunction engineering of these structures and the control achieved in obtaining desirable wavefunction localization. We show that when combined with optimization methods, wavefunction engineering provides a powerful new methodology for the optimized design of optoelectronic devices.

Contents

1. Introduction

There have been remarkable advances over the past few decades in the development of optoelectronic devices. In particular, quantum well lasers, emitting with wavelengths from the near-UV, blue, red, the mid-IR region (2–8 μm), all the way to the far-IR ($\sim$100 μm) region of the spectrum, have been successfully demonstrated. This spectacular evolution since the development of GaAs quantum well lasers in the early 1970s has been achieved by means of technological improvements in the growth of structures. In the following, we are concerned with the electronic properties of the III–V and II–VI compound semiconductors and their heterostructures [1].

The geometry of the layered structure, i.e., the layer thicknesses in the multi-quantum well structure, plays a key role in determining the effective energy bandgap of the heterostructure, which arises as a manifestation of the Heisenberg uncertainty principle and carrier localization. This insight was distilled into the concept of 'bandgap engineering'. By choosing different materials with suitable energy bandgaps for individual layers, bandgap engineering has provided a conceptual framework for designing heterostructures with specific optical properties [2].

Through a combination of computational modelling and advances in the growth of materials, we can progress considerably further today in exploring the details of the carrier wavefunctions, how they are shaped by choices for materials in the individual layers, and the layer geometry. We are essentially tailoring the localization and distribution of the wavefunctions in the heterostructure, and optimizing optical transition matrix elements, which fundamentally determine the response and operation of the optoelectronic device. In this article, we provide a theoretical and computational overview of these advances within the framework of what we term as *wavefunction engineering* [3].

We have emphasized earlier [4] that the finite element method (FEM) can be employed to advantage in simulating the electronic energy band structures of semiconductor heterostructures. The FEM [3, 5] may be considered to be the discretization of the action integral, which is fundamental to all of physics through its use in the principle of least action. We show that the Schrödinger Lagrangian (rather than the Hamiltonian), in conjunction with the action integral, provides specific advantages in that we can of course obtain the equation of motion, the Schrödinger equation. We can advance further in this framework by employing a gauge-variational method to obtain the conserved current and the current continuity boundary conditions at interfaces [6] in an unambiguous manner, and include perturbations such as the built-in strain in the heterostructure and externally applied electric and magnetic fields in a natural manner. Again, the Lagrangian may be used in a discretized action in FEM calculations to obtain wavefunctions and momentum matrix elements. In the layered structure, each layer contributes additively to the global action integral. Finally, the effect of charge redistributions in doped heterostructures due to ionized impurity dopants and free carriers, leading to energy bandedge bending, can be accounted for using the FEM. This ubiquitous problem of the Schrödinger–Poisson self-consistency occurs in essentially all active devices, and the FEM provides a convergent, stable solution in tens of iterations [7] for arbitrary layered heterostructures with arbitrary doping profiles.

When combined with computational optimization routines the FEM allows us to predict the material properties and optimized geometry of structures under bias that can have the desired energy level structure necessary for laser emission at *specific* wavelengths. In this

sense, wavefunction engineering has matured to a level where we can *predict* the optoelectronic properties of a given heterostructure, and furthermore provide reliable guidelines for the growth of heterostructures having specific desired outcomes in terms of their optoelectronic response [8].

This review is organized as follows. In section 2, we describe the $\mathbf{k}\cdot\mathbf{P}$ model Lagrangian used to calculate the band structure of heterostructures. In section 3, we show how the wavefunction and current continuity boundary conditions are derived consistent with operator ordering. We give examples of wavefunction engineering in section 4. We compare the present methodology with other band structure modelling in section 5, and provide concluding remarks in section 6.

2. A Lagrangian formulation of the valence band structure

For our purposes here, in the envelope function approximation (EFA), the general form of the wavefunction may be considered to be a linear combination of a finite number of band wavefunctions, indexed by n, of the form

$$\psi(r) = f_n(z)\mathrm{e}^{\mathrm{i}k_x x}\mathrm{e}^{\mathrm{i}k_y y}u_n(r) \equiv F_n(r)\,u_n(r). \tag{1}$$

A clear perspective on the formulation of the band structure arises on using the principle of least action in setting up the $\mathbf{k}\cdot\mathbf{P}$ model [9]. A number of issues such as derivative operator-ordering are resolved in a very natural manner, leading to a number of insights into the approximations that are invoked in the modelling. The action integral that leads to the Schrödinger equation for the valence bands is given by

$$\mathbf{A} = \int \mathrm{d}t \int_V \mathrm{d}^3 r \left(F_n^*(r)u_n^*(r)\right)\left[\overleftarrow{\partial}\frac{\hbar^2}{2m_0}\vec{\partial} + (V(r)-E)\right](F_n(r)u_n(r)) = \int \mathrm{d}t \int \mathrm{d}^3 r \mathbf{L}\,. \tag{2}$$

The directed derivatives $\overleftarrow{\partial}$ and $\vec{\partial}$ act on the functions appearing to the left and to the right, respectively. All the bands are treated within degenerate perturbation theory. In the following, the integral over time is irrelevant since we are concerned with the time-independent band structure problem.

Within the spirit of the EFA, we perform 'cell-averaging' by integrating over each unit cell in the crystal. The envelope functions $F_n(r)$ are typically considered to be slowly varying functions whereas the cell-periodic, and more oscillatory, Bloch functions satisfy Schrödinger's equation with band-edge energies. We use the results:

$$\begin{aligned}&\int_{\text{cell}} \mathrm{d}^3 r\, u_n^*(r)u_{n'}(r) = \delta_{nn'};\\ &\int_{\text{cell}} \mathrm{d}^3 r \left[\nabla u_n^*(r)\frac{\hbar^2}{2m_0}\nabla u_{n'}(r) + u_n^*(r)V(r)u_{n'}(r)\right] = E_n\delta_{nn'},\end{aligned} \tag{3}$$

and write the momentum matrix element between Bloch states as

$$\int_{\text{cell}} \mathrm{d}^3 r u_n^*(r)\nabla u_{n'}(r) = \frac{\mathrm{i}}{\hbar}\mathbf{p}_{nn'} = -\int_{\text{cell}} \mathrm{d}^3 r \nabla u_n^*(r)u_{n'}(r), \qquad n \neq n'. \tag{4}$$

The cell-averaged action integral can then be written in terms of the envelope functions alone, and we have

$$\begin{aligned}\langle\mathbf{A}\rangle = \int \mathrm{d}t \int \mathrm{d}^3 r \Bigg(&\nabla F_n^*\frac{\hbar^2}{2m_0}\nabla F_{n'} + \frac{\mathrm{i}\hbar}{2m_0}\left\{F_n^*\overleftarrow{\partial}F_{n'}\,\mathbf{p}_{nn'} - \mathbf{p}_{nn'}F_n^*\vec{\partial}F_{n'}\right\}\\ &+ \delta_{nn'}F_n^*(E_n - E)F_{n'}\Bigg).\end{aligned} \tag{5}$$

The integrand in large parentheses in the above equation, the Lagrangian density $\langle \mathbf{L} \rangle$, may be cast in a matrix form by separating the band index n into the valence v, and the energetically higher remote bands with an index r. Following Lowdin's perturbation theory [10], we eliminate the remote band wavefunctions in favour of the valence bands of interest by employing the equations of motion for the remote bands. If we had been developing the bulk $\mathbf{k} \cdot \mathbf{P}$ theory, the following terms would correspond to the Kane model [1, 9] for the band structure, with terms quadratic in the derivatives ($O(k^2)$ terms) within the valence bands. Ignoring spin for the moment, we have

$$\langle \mathbf{L} \rangle_{vv'} = F_v^* \left[\overleftarrow{\partial} \frac{\hbar^2}{2m_0} \vec{\partial} + (E_v - E)\delta_{vv'} \right] F_{v'} + \left(\frac{\hbar^2}{m_0^2} \right) \sum_r F_v^* \overleftarrow{\partial} \mathbf{p}_{vr} \frac{1}{(E - E_r)} \mathbf{p}_{rv'} \vec{\partial} F_{v'}, \qquad \{v, v' = X, Y, Z\}, \tag{6}$$

where the p-like valence Bloch states in the III–V and II–VI semiconductors have been denoted by their symmetry-specified form in terms of X, Y and Z. We have neglected terms of higher order in perturbation theory and used Lowdin's approximations. The advantage of the above derivation is that it explicitly retains the order of the derivative operators, each term in the Lagrangian is Hermitian, and there is no ambiguity about reordering of operators for symmetrization. The focus is on the bands in the immediate vicinity of the bandgaps of the III–V or II–VI materials. We now follow Kane's discussion for the evaluation of the contributions of the remote bands to the valence bands. Extensions to include the conduction bands follow schemes used earlier by explicitly subtracting the contribution of the conduction band states from the Luttinger γ parameters [11, 12].

2.1. The zinc blende semiconductors

The possible intermediate states contributing to the Γ_{15} valence states belong to the energetically higher conduction bands of symmetry Γ_1 (s-like states), Γ_{12} states of symmetry $\{2z^2 - x^2 - y^2, \sqrt{3}(x^2 - y^2)\}$, Γ_{15} states of the form $\{yz, zx, xy\}$, and the Γ_{25} states. These states are compatible with the atomic s, p, d, and f orbital contributions to the valence electronic structure of semiconductors, respectively. It has been estimated that the contribution of the f orbitals to the valence electronic bands in semiconductors is negligible and hence the Γ_{25} intermediate states will be ignored. Following the notation of Foreman [13], we define

$$\sigma = -(1/3m_0) \sum_r^{\Gamma_1} |\langle X|p_x|u_r\rangle|^2/(E_v - E_r),$$

$$\pi = -(1/3m_0) \sum_r^{\Gamma_{15}} |\langle X|p_y|u_r\rangle|^2/(E_v - E_r),$$

and

$$\delta = -(1/6m_0) \sum_r^{\Gamma_{12}} \langle X|p_x|u_r\rangle|^2/(E_v - E_r). \tag{7}$$

We then determine the contributions to the individual matrix elements of $\langle \mathbf{L} \rangle_{vv'}$. The matrix of derivative operators that act on the envelope functions $\{F_{vx}, F_{vy}, F_{vz}\}$ can be shown to be of the form

$$\langle \mathbf{L} \rangle_{vv'} = \left(\frac{\hbar^2}{2m_0} \right)$$

$$\times \begin{bmatrix} \left\{ \begin{matrix} \overleftarrow{\partial}_x A \vec{\partial}_x + \overleftarrow{\partial}_y B \vec{\partial}_y \\ + \overleftarrow{\partial}_z B \vec{\partial}_z + E_v - E \end{matrix} \right\} & \overleftarrow{\partial}_x C_1 \vec{\partial}_y - \overleftarrow{\partial}_y C_2 \vec{\partial}_x & \overleftarrow{\partial}_x C_1 \vec{\partial}_z - \overleftarrow{\partial}_z C_2 \vec{\partial}_x \\ \overleftarrow{\partial}_y C_1 \vec{\partial}_x - \overleftarrow{\partial}_x C_2 \vec{\partial}_y & \left\{ \begin{matrix} \overleftarrow{\partial}_y A \vec{\partial}_y + \overleftarrow{\partial}_z B \vec{\partial}_z \\ + \overleftarrow{\partial}_x B \vec{\partial}_x + E_v - E \end{matrix} \right\} & \overleftarrow{\partial}_y C_1 \vec{\partial}_z - \overleftarrow{\partial}_z C_2 \vec{\partial}_y \\ \overleftarrow{\partial}_z C_1 \vec{\partial}_x - \overleftarrow{\partial}_x C_2 \vec{\partial}_z & \overleftarrow{\partial}_z C_1 \vec{\partial}_y - \overleftarrow{\partial}_y C_2 \vec{\partial}_z & \left\{ \begin{matrix} \overleftarrow{\partial}_z A \vec{\partial}_z + \overleftarrow{\partial}_x B \vec{\partial}_x \\ + \overleftarrow{\partial}_y B \vec{\partial}_y + E_v - E \end{matrix} \right\} \end{bmatrix}, \tag{8}$$

in the envelope function basis. Here $A = 1 - 6\sigma - 12\delta$, $B = 1 - 6\pi$, $C_1 = 6\delta - 6\sigma$, and $C_2 = 6\pi$. While in the *bulk* semiconductor (where the envelope functions are of the form $\exp(\mathrm{i}\mathbf{k}\cdot\mathbf{r})$) the ordering of the derivative operators is redundant [9, 14], and the way in which the band parameters are grouped is irrelevant, it becomes crucial in the heterostructure. The interface boundary conditions depend on the particular ordering of the differentiation operators relative to the band parameters that vary across the interface. The parameters σ, δ and π are simply related to the usual Luttinger parameters [14] and we have $\gamma_1 = -1 + 2\sigma + 4\pi + 4\delta$, $\gamma_2 = \sigma - \pi + 2\,\delta$, and $\gamma_3 = \sigma + \pi - \delta$. The three parameters based on the symmetry type can be determined from experiments, as are the Luttinger parameters, so that the implementation of envelope function continuity and the probability current continuity conditions at interfaces now becomes feasible [15, 16]. The inclusion of the electron spin and the effects of spin–orbit interaction are straightforward and we obtain a 6×6 valence Lagrangian. The spin–orbit interaction splits the six-fold degeneracy at the zone centre into a four-fold degenerate heavy-hole (hh) and light-hole (lh) bands of Γ_8 symmetry with total angular momentum $J = 3/2$, and a doubly degenerate split-off (so) band of Γ_7 symmetry. The valence Lagrangian in the $|J, m_j\rangle$ basis is given by

$$\mathsf{L}_{vv'} = \begin{bmatrix} P+Q & -S_- & R & 0 & \frac{-1}{\sqrt{2}}S_- & \sqrt{2}R \\ -\tilde{S}_+ & P-Q & C_- & R & -\sqrt{2}Q & \Sigma_- \\ R^* & -C_+ & P-Q & -\tilde{S}_- & \Sigma_+ & \sqrt{2}Q \\ 0 & R^* & S_+ & P+Q & -\sqrt{2}R^* & -\frac{1}{\sqrt{2}}S_+ \\ -\frac{1}{\sqrt{2}}\tilde{S}_+ & -\sqrt{2}Q & -\tilde{\Sigma}_- & -\sqrt{2}R & P+\Delta & \tilde{C}_- \\ \sqrt{2}R^* & -\tilde{\Sigma}_+ & \sqrt{2}Q & \frac{1}{\sqrt{2}}\tilde{S}_- & -\tilde{C}_+ & P+\Delta \end{bmatrix} \begin{matrix} |\frac{3}{2}, \frac{3}{2}\rangle \\ |\frac{3}{2}, \frac{1}{2}\rangle \\ |\frac{3}{2}, -\frac{1}{2}\rangle \\ |\frac{3}{2}, -\frac{3}{2}\rangle \\ |\frac{1}{2}, \frac{1}{2}\rangle \\ |\frac{1}{2}, -\frac{1}{2}\rangle \end{matrix}, \tag{9}$$

where, specializing to the case of the [001] growth direction, we have

$$\begin{aligned} &P = \gamma_1 k_\parallel^2 + \overleftarrow{\partial}_z \gamma_1 \vec{\partial}_z - (E_v - E); \qquad Q = \gamma_2 k_\parallel^2 - 2\overleftarrow{\partial}_z \gamma_2 \vec{\partial}_z, \\ &R = -\sqrt{3}\gamma_2 \left(k_x^2 - k_y^2\right) + \mathrm{i}2\sqrt{3}\gamma_3 k_x k_y; \qquad S_\pm = \frac{\mathrm{i}}{\sqrt{3}}\left[k_\pm C_1 \vec{\partial}_z + \overleftarrow{\partial}_z C_2 k_\pm\right], \\ &\Sigma_\pm = \frac{\mathrm{i}}{3\sqrt{2}}\left[\overleftarrow{\partial}_z (C_2 - 2C_1)\, k_\pm + k_\pm (C_1 - 2C_2)\vec{\partial}_z\right]; \\ &C_\pm = \frac{-\mathrm{i}}{\sqrt{3}}\left[k_\pm (C_1 + C_2)\vec{\partial}_z + \overleftarrow{\partial}_z (C_1 + C_2) k_\pm\right]. \end{aligned} \tag{10}$$

Here $\{\gamma_1, \gamma_2, \gamma_3, C_1, C_2\}$ are in units of $(\hbar^2/2m_0)$ and $k_\pm = k_x \pm \mathrm{i}k_y$. The quantities $S_\pm$, $C_\pm$, $\Sigma_\pm$ and $\tilde{S}_\pm$, $\tilde{C}_\pm$, $\tilde{\Sigma}_\pm$ differ by the exchange of the location of the directed derivatives and k-components in the expressions. *Thus, the Hermiticity of the Lagrangian can be verified with more care than is usually needed.* All the parameters introduced above are expressible in terms of the three quantities σ, δ, and π, or equivalently, in terms of the Luttinger γ parameters. In the bulk semiconductor, we have $\tilde{S}_+ = -S^+$, $\Sigma_- = \sqrt{3/2}S_-$, and $C_\pm = 0$. Thus, the operator ordering leads to the breaking up of the usual parameters into component contributions that appear to contribute differently in layered systems as compared with bulk

semiconductors. Additional perturbations, e.g. the strain energy, are additively included in the Lagrangian [15, 16].

2.2. *The wurtzite semiconductors*

We consider the bands in the immediate vicinity of the bandgap of wurtzite materials at the zone centre. The valence states belong to the $\{\Gamma_{5v} : \{X, Y\} + \Gamma_{1v} : \{Z\}\}$ representations. The deeper valence bands belong to the $\Gamma_{6v} : \{X^2 - Y^2, 2XY\}$ and the $\Gamma_{1v} : \{Z\}$ representations. The nearest higher conduction bands belong to the Γ_{5c} states of $\{X, Y\}$ symmetry and the Γ_{3c} states transform as the $\{Z\}$ representation. Here we are using the notation of [17], for example.

The second-order valence band terms of (6) are evaluated as done by Kane for bulk zinc blende semiconductors. We define parameters for the contributions of the higher Γ_{1c} conduction bands as follows:

$$\sigma_1 = \frac{1}{m_0}\sum_{\Gamma_1}\langle\Gamma_5^{\left\{\begin{smallmatrix}X\\Y\end{smallmatrix}\right\}}|p_{X,Y}|\Gamma_1^{\{S\}}\rangle|^2/(E_v - E_{\Gamma_1});$$

$$\sigma_2 = \frac{1}{m_0}\sum_{\Gamma_1}|\langle\Gamma_1^{\{Z\}}|p_Z|\Gamma_1^{\{S\}}\rangle|^2/(E_v - E_{\Gamma_1}),$$

and

$$\sigma_3 = \frac{1}{m_0}\sum_{\Gamma_1}\langle\Gamma_5^{\left\{\begin{smallmatrix}X\\Y\end{smallmatrix}\right\}}|p_{X,Y}|\Gamma_1^{\{S\}}\rangle\langle\Gamma_1^{\{S\}}|p_Z|\Gamma_1^{\{Z\}}\rangle/(E_v - E_{\Gamma_1}). \tag{11}$$

The Γ_{3c} intermediate conduction states do not contribute to the valence bands. The contribution of the $\Gamma_5\{XZ, YZ\}$ intermediate states can be parameterized by writing

$$\delta_1 = \frac{1}{m_0}\sum_{\Gamma_5}|\langle\Gamma_5^{\left\{\begin{smallmatrix}X\\Y\end{smallmatrix}\right\}}|p_Z|\Gamma_5^{\left\{\begin{smallmatrix}XZ\\YZ\end{smallmatrix}\right\}}\rangle|^2/(E_v - E_{\Gamma_5});$$

$$\delta_2 = \frac{1}{m_0}\sum_{\Gamma_5}|\langle\Gamma_1^{\{Z\}}|p_{X,Y}|\Gamma_5^{\left\{\begin{smallmatrix}XZ\\YZ\end{smallmatrix}\right\}}\rangle|^2/(E_v - E_{\Gamma_5}),$$

and

$$\delta_3 = \frac{1}{m_0}\sum_{\Gamma_5}\langle\Gamma_1^{\{Z\}}|p_{X,Y}|\Gamma_5^{\left\{\begin{smallmatrix}XZ\\YZ\end{smallmatrix}\right\}}\rangle\langle\Gamma_5^{\left\{\begin{smallmatrix}XZ\\YZ\end{smallmatrix}\right\}}|p_Z|\Gamma_5^{\left\{\begin{smallmatrix}X\\Y\end{smallmatrix}\right\}}\rangle/(E_v - E_{\Gamma_5}). \tag{12}$$

The Γ_6 states of symmetry $\{X^2 - Y^2, 2XY\}$ require an additional parameter to represent their contribution. We define

$$\lambda = \frac{1}{m_0}\sum_{\Gamma_6}|\langle\Gamma_5^{\{X,Y\}}|p|\Gamma_6^{\left\{\begin{smallmatrix}X^2-Y^2\\2XY\end{smallmatrix}\right\}}\rangle|^2/(E_v - E_{\Gamma_6}). \tag{13}$$

The valence band Lagrangian for the wurtzite crystal, in the $\{X, Y, Z\}$ basis, is now given by [18, 19]

$$\langle\mathbf{L}\rangle_{vv'} = \begin{bmatrix} \left\{\begin{smallmatrix}\overleftarrow{\partial}_x L_1\vec{\partial}_x + \overleftarrow{\partial}_y M_1\vec{\partial}_y\\ + \overleftarrow{\partial}_z M_2\vec{\partial}_z + (E_v - E)\end{smallmatrix}\right\}, & \overleftarrow{\partial}_x\tilde{N}_1\vec{\partial}_y + \overleftarrow{\partial}_y\tilde{N}_1'\vec{\partial}_x, & \overleftarrow{\partial}_x\tilde{N}_2\vec{\partial}_z + \overleftarrow{\partial}_z\tilde{N}_2'\vec{\partial}_x \\ \overleftarrow{\partial}_y\tilde{N}_1\vec{\partial}_x + \overleftarrow{\partial}_x\tilde{N}_1'\vec{\partial}_y, & \left\{\begin{smallmatrix}\overleftarrow{\partial}_x M_1\vec{\partial}_x + \overleftarrow{\partial}_y L_1\vec{\partial}_y\\ + \overleftarrow{\partial}_z M_2\vec{\partial}_z + (E_v - E)\end{smallmatrix}\right\}, & \overleftarrow{\partial}_y\tilde{N}_2\vec{\partial}_z + \overleftarrow{\partial}_z\tilde{N}_2'\vec{\partial}_y \\ \overleftarrow{\partial}_z\tilde{N}_2\vec{\partial}_x + \overleftarrow{\partial}_x\tilde{N}_2'\vec{\partial}_z, & \overleftarrow{\partial}_z\tilde{N}_2\vec{\partial}_y + \overleftarrow{\partial}_y\tilde{N}_2'\vec{\partial}_z, & \left\{\begin{smallmatrix}\overleftarrow{\partial}_x M_3\vec{\partial}_x + \overleftarrow{\partial}_y M_3\vec{\partial}_y\\ + \overleftarrow{\partial}_z L_2\vec{\partial}_z + (E_v - E)\end{smallmatrix}\right\} \end{bmatrix}, \tag{14}$$

where the parameters L_i, M_i, and N_i are given by

$$\begin{aligned} &L_1 = 1 - 2\sigma_1 - 4\lambda; \qquad L_2 = 1 - 2\sigma_2; \qquad \tilde{N}_1 = -2\sigma_1 + 4\lambda; \\ &\tilde{N}_1' = -4\lambda; \qquad \tilde{N}_2 = -2\sigma_3; \qquad \tilde{N}_2' = -2\delta_3; \\ &M_1 = 1 - 4\lambda; \qquad M_2 = 1 - 2\delta_1; \qquad M_3 = 1 - 2\delta_2, \end{aligned} \tag{15}$$

in units of $\hbar^2/2m_0$. The order of the derivative operators with $\tilde{N}_1'$ and $\tilde{N}_2'$ terms is reversed with respect to $\tilde{N}_1$ and $\tilde{N}_2$ terms. In the bulk semiconductor, the operator ordering is irrelevant and we obtain the bulk parameters $N_1 \equiv \tilde{N}_1 + \tilde{N}_1'$ and $N_2 \equiv \tilde{N}_2 + \tilde{N}_2'$. Furthermore, as has been shown by Chuang and Chang [20], the six-fold symmetry under rotation about the c-axis leads to the relation $(L_1 - M_1) = N_1$.

The valence band edge is not triply degenerate in wurtzite semiconductors, and the crystal field splitting leads to the shifts in the band edge energy E_v by $\langle X|L_{(\mathrm{c.f.})}|X\rangle = \langle Y|L_{(\mathrm{c.f.})}|Y\rangle = \Delta_1$, and $\langle Z|L_{(\mathrm{c.f.})}|Z\rangle = 0$. The spin–orbit splitting, generated by

$$\begin{aligned} L_{\mathrm{so}} &= \frac{\hbar}{4m_0^2c^2}\nabla V \times \mathbf{p}\cdot\boldsymbol{\sigma} \\ &= L_{(\mathrm{so})x}\sigma_x + L_{(\mathrm{so})y}\sigma_y + L_{(\mathrm{so})z}\sigma_z, \end{aligned} \tag{16}$$

is parameterized by the relations [20]

$$\langle X|L_{(\mathrm{so})z}|Y\rangle = -\mathrm{i}\Delta_2; \qquad \langle Y|L_{(\mathrm{so})x}|Z\rangle = \langle Z|L_{(\mathrm{so})y}|X\rangle = -\mathrm{i}\Delta_3. \tag{17}$$

The spinor matrix elements of the standard Pauli spin matrices $\boldsymbol{\sigma}$ are readily included in the above derivation. With these definitions in place, we consider the inclusion of spin in the Lagrangian. We make the same choice as in [20] for the valence band basis states with spin. The valence band Lagrangian, including the crystal-field splitting and the spin–orbit interaction, is given by

$$\mathbf{L}_{vv'} = \begin{bmatrix} P & -K^* & \tilde{S}_- & 0 & 0 & 0 \\ -K & Q & -\tilde{S}_+ & 0 & 0 & \Delta \\ -S_+ & S_- & R & 0 & \Delta & 0 \\ 0 & 0 & 0 & P & -K & -\tilde{S}_+ \\ 0 & 0 & \Delta & -K^* & Q & \tilde{S}_- \\ 0 & \Delta & 0 & S_- & -S_+ & R \end{bmatrix}, \tag{18}$$

where, specializing to the case of the [0001] growth direction, and switching the sign of the energy to be positive for the valence bands, we have

$$\begin{aligned} &P = (\Delta_1 + \Delta_2 + E_v - E) + \alpha; \qquad Q = (\Delta_1 - \Delta_2 + E_v - E) + \alpha, \\ &R = \left[\overleftarrow{\partial}_z A_1 \vec{\partial}_z + A_2 k_\parallel^2\right] + (E_v - E); \qquad K = A_5(k_x + \mathrm{i}k_y)^2, \\ &S_\pm = \frac{\mathrm{i}}{\sqrt{2}}[\overleftarrow{\partial}_z N_2 k_\pm - k_\pm N_2' \vec{\partial}_z]; \qquad \tilde{S}_\pm = \frac{-\mathrm{i}}{\sqrt{2}}[\overleftarrow{\partial}_z N_2' k_\pm - k_\pm N_2 \vec{\partial}_z], \\ &\alpha = \left[\overleftarrow{\partial}_z (A_1 + A_3)\vec{\partial}_z + (A_2 + A_4)k_\parallel^2\right]; \qquad \Delta = \sqrt{2}\Delta_3. \end{aligned} \tag{19}$$

Here the Bir–Pikus parameters [18] are identified by the relations

$$\begin{aligned} &A_1 = L_2; \qquad A_2 = M_3; \\ &A_3 = M_2 - L_2; \qquad A_4 = (L_1 + M_1)/2 - M_3; \\ &A_5 = (\tilde{N}_1 + \tilde{N}_1')/2; \qquad A_6 = (\tilde{N}_2 + \tilde{N}_2')/\sqrt{2}. \end{aligned} \tag{20}$$

The parameter A_6 does not appear in the Lagrangian and instead we have to contend with the determination of two separate parameters ($\tilde{N}_2$ and $\tilde{N}_2'$) in order to proceed. This requires that one of the parameters σ_3 or δ_3 (see (11) and (12)) be known from *ab initio* calculations. We

have tentatively used $\delta_3 = \delta_1$. Mireles and Ulloa [21] have one parameter less in their analysis. The quantities $S_\pm$ and $\tilde{S}_\pm$ differ by the exchange of the location of the directed derivatives and k-components in the expressions.

The inversion asymmetry terms [22] in the wide-gap wurtzite semiconductors have been shown to provide an improved description of the valence bands. The valence band parameter A_7 has been expressed in the convenient form $A_7 = (-\mathrm{i}\hbar/m_0\sqrt{2})\langle X|p_x|Z\rangle$ by Dugdale *et al* [23]. A detailed accounting of the various contributions from band mixing and the admixture of d-orbitals to the inversion asymmetry parameter has been given by Lew Yan Voon *et al* [17]. In the $\{XYZ\}$ orbital basis we have

$$\mathbf{L}_{\mathrm{inv}} = \begin{pmatrix} 0 & 0 & \mathrm{i}\sqrt{2}A_7k_x \\ 0 & 0 & \mathrm{i}\sqrt{2}A_7k_y \\ -\mathrm{i}\sqrt{2}A_7k_x & -\mathrm{i}\sqrt{2}A_7k_y & 0 \end{pmatrix}. \tag{21}$$

This 3×3 valence band matrix is doubled to accommodate the spin degree of freedom and the resulting 6×6 Lagrangian is added to the valence band Lagrangian in (18).

3. Interface boundary conditions for current continuity

The action integral is varied with respect to the envelope functions F^* and the principle of least action is invoked to derive the six coupled Schrödinger differential equations in the six-band zinc blende $\mathbf{k}\cdot\mathbf{P}$ model. Similar considerations hold for the wurtzite materials. In the following, we simplify the discussion of the boundary conditions by considering just the valence bands *without including spin*, with the Lagrangian given by (8). In a layered heterostructure, each layer contributes a piece of the action integral. The material properties change across layer interfaces and we attach a layer index λ to each of the parameters A, B, C_1, and C_2 appearing in (8). With the layer growth along the z-axis, the terms in the Lagrangian are separated into those with different numbers of directed derivatives in z. The action integral takes the form

$$\mathbf{A} = \int \mathrm{d}t \sum_\lambda \int_{z_\lambda}^{z_{\lambda+1}} \mathrm{d}z F_i^* \left[\overleftarrow{\partial}_z \mathbf{K}^{(\lambda)} \vec{\partial}_z + (\overleftarrow{\partial}_z \mathbf{Q}^{(\lambda)} + \mathbf{Q}^{(\lambda)+} \vec{\partial}_z) + \mathbf{R}^{(\lambda)} + (E_i^{(\lambda)}\delta_{ij} - E)\mathbf{1} \right] F_j. \tag{22}$$

Here the unit matrix is denoted by $\mathbf{1}$, and the other matrix coefficients in the Lagrangian are given by

$$\mathbf{K}^{(\lambda)} = \begin{bmatrix} B^{(\lambda)} & 0 & 0 \\ 0 & B^{(\lambda)} & 0 \\ 0 & 0 & A^{(\lambda)} \end{bmatrix}, \qquad \mathbf{Q}^{(\lambda)} = \begin{bmatrix} 0 & 0 & -\mathrm{i}k_x C_2^{(\lambda)} \\ 0 & 0 & -\mathrm{i}k_y C_2^{(\lambda)} \\ \mathrm{i}k_x C_1^{(\lambda)} & \mathrm{i}k_y C_1^{(\lambda)} & 0 \end{bmatrix},$$

and

$$\mathbf{R}^{(\lambda)} = \begin{bmatrix} (A^{(\lambda)}k_x^2 + B^{(\lambda)}k_y^2) & (C_1^{(\lambda)} - C_2^{(\lambda)})k_xk_y & 0 \\ (C_1^{(\lambda)} - C_2^{(\lambda)})k_xk_y & (B^{(\lambda)}k_x^2 + A^{(\lambda)}k_y^2) & 0 \\ 0 & 0 & B^{(\lambda)}(k_x^2 + k_y^2) \end{bmatrix}. \tag{23}$$

Observe that while the individual linear derivative term $\mathbf{Q}$ is not Hermitian by itself, the combination of the two terms involving $\mathbf{Q}$ and $\mathbf{Q}^+$ together is Hermitian. One of the boundary conditions at interfaces is the continuity of the envelope wavefunction. The second boundary condition at the interfaces is the continuity of the probability current across the interfaces, which we evaluate using a gauge-variational approach that is common in particle physics. Following Gell-Mann and Levy [6], we substitute $F_j(z) \to \mathrm{e}^{\mathrm{i}\Lambda(z)}F_j(z)$ in the Lagrangian (22)

and develop a variation of the Lagrangian with respect to the gauge function $\Lambda(z)$. In the presence of operator ordering, the conserved current is obtained in the form

$$\mathbf{J} = \frac{1}{\hbar}\left(\frac{\delta\langle \mathbf{L}\rangle}{\delta(\partial_z \Lambda)}\right)\Bigg|_{\Lambda=0} = \frac{\mathrm{i}}{\hbar}\left[-F_i^* \mathbf{K}_{\mathbf{ij}}^{(\lambda)} \partial_z F_j + (\partial_z F_i^*)\mathbf{K}_{\mathbf{ij}}^{(\lambda)} F_j - F_i^* \mathbf{Q}_{\mathbf{ij}}^{(\lambda)} F_j + F_i^* \mathbf{Q}_{\mathbf{ij}}^{(\lambda)+} F_j\right]. \tag{24}$$

The continuity conditions at an interface at $z = 0$ are then given by $F|_{0^-} = F|_{0^+}$, and

$$\mathbf{K}F' + \mathbf{Q}F|_{0^-} = \mathbf{K}F' + \mathbf{Q}F|_{0^+}.$$

4. Examples of wavefunction engineering of quantum heterostructures

The discretized Schrödinger equation is obtained by the FEM, which may be thought of as the discretization of the action integral [5]. The physical region is split into small regions, finite elements, in each layer, and the wavefunctions are expressed in terms of interpolation polynomials with as-yet unknown coefficients in each finite element. The spatial dependence is integrated out, and the element matrices are overlaid in a global matrix, for the structure as a whole, in order to ensure that the continuity conditions discussed in section 3 are implemented. We minimize the action by varying the unknown coefficients. The resulting discretized Schrödinger matrix equation is solved by sparse matrix methods. This approach ties in the action to the numerical work and provides a systematic approach to improving the variational solution. The contributions of specific layers can be emphasized in FEM by discretizing them appropriately. We have applied this method to obtain the energy eigenvalues and wavefunctions in heterostructures, in-plane energy dispersions, and optical matrix elements. The method is also extended to obtain a self-consistent solution to the Schrödinger–Poisson problem of band bending [7], a problem of particular interest in the context of spintronics applications where the carrier concentrations in GaMnAs, for example, can be as high as $\sim 10^{20}$ cm^{-3} [24]. In the following, we consider examples of finite element modelling of heterostructures of common interest. The calculations make use of the band parameters given in [25].

In figure 1, the evolution of the design of a heterostructure for a mid-IR laser is shown. The initial type-II quantum well structure in figure 1(a) has poor conduction band (Ψ_n) and valence band (Ψ_p) wavefunction overlap for optical matrix elements. By introducing another layer in the well to form a step potential, as in figure 1(b), the wavefunctions are better confined and show increased overlap. With yet another layer, we obtain the so-called W-structure, shown in figure 1(c). The W-structure was grown to specifications based on wavefunction engineering, and the very first structure grown exhibited lasing in the mid-IR region (4 μm) of the spectrum. This is a classic example of wavefunction engineering [4, 26] through which we are able to manipulate the material properties of the structure to obtain desired wavefunctions and design a working laser to operate at expected wavelengths. The W-laser holds the present record for continuous operation up to 275 K for mid-IR lasers.

In figure 2(a), we show the band bending in a modulation-doped single quantum well, comparing the bandedge profile before and after the self-consistent calculation, with the rate of convergence for the Schrödinger–Poisson calculation shown in figure 2(b) [7]. Figure 2(c) shows the first heavy hole wavefunction before (dotted lines) and after (solid lines) the hole redistribution. If only the original band offset potential is considered, the wavefunction is of the simple cosine-like form. When the self-consistent potential is included, the total potential resembles that of a double quantum well, and the heavy hole wavefunction reflects this by having two peaks. In more complex situations, the doping profile can be controlled to shape the wavefunctions differently, a situation that may be termed wavefunction engineering by modulation doping.

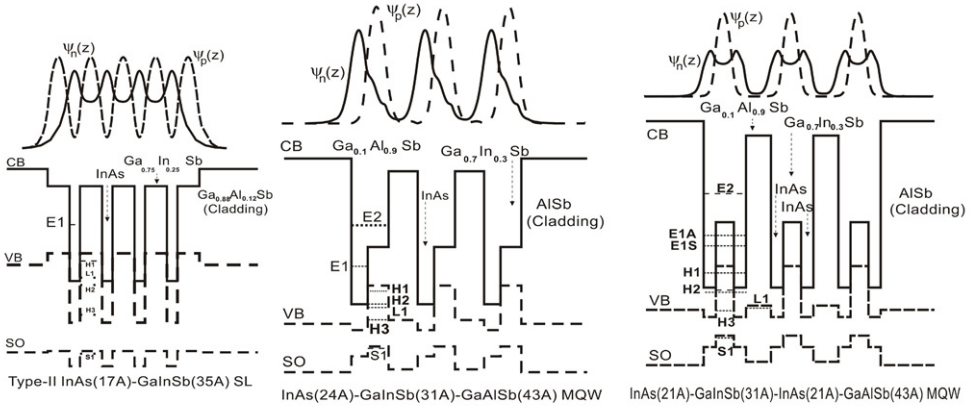

Figure 1. (a) The type-II heterostructure of InAs/GaInSb leads to localization of wavefunctions in different layers. This is ameliorated partially by introducing a step potential as in (b). The W-structure, shown in (c), provides a substantially improved overlap (figure adapted from [4, 26]; with permission from Elsevier).

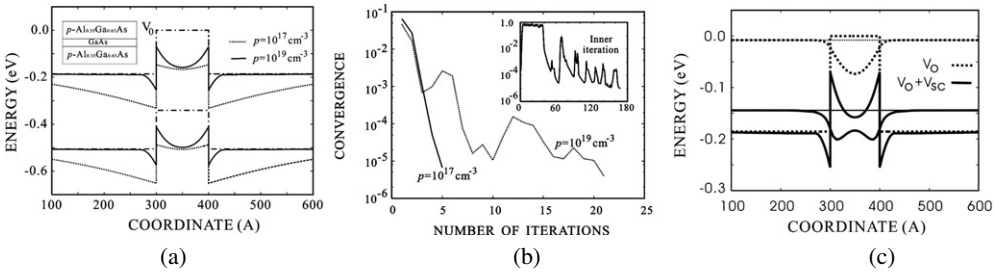

Figure 2. The valence band bending in a quantum well with p-doped barriers is shown. The FEM iterations for the Schrödinger–Poisson calculations converge to the self-consistent solution in a stable manner to the band profile shown in (a), in very few iterations as shown in (b), in the dual-loop algorithm of [7]. The wavefunctions in the double well created by the self-consistent band bending are shown in (c) (after [7]).

The $ZnSe/Zn_{1-x}Mn_xSe$ multilayer system was reported [27] to form a spin superlattice. For $x \sim 0.04$, the conduction bandedge of ZnSe is almost the same as that of the diluted magnetic semiconductor (DMS) $Zn_{1-x}Mn_xSe$. In an applied magnetic field, the Mn spins are aligned and the effective conduction bandedge of ZnMnSe for spin-up electrons is higher than that of ZnSe. It is the opposite for spin-down electrons, so that the spin-up electrons are localized in the ZnSe layer and spin-down electrons in the ZnMnSe layer. In figure 3(a), we plot the effective bandedge and the wavefunction for the lowest spin-down electron Landau level, and in figure 3(b), for the lowest spin-up level, at $B = 5$ T.

When the Mn alignment is not considered, by neglecting the DMS Lagrangian for the DMS layer (dotted lines), the probability that the electrons reside in the ZnSe layer is 51.4% for both spin-up and spin-down electrons due to a small conduction band offset. When the Mn alignment is taken into account by including the DMS Lagrangian for the ZnMnSe layer, the probability becomes 42.1% for spin-down electrons and 60.6% for spin-up electrons. Thus the Mn alignment through an external magnetic field alters the localization of spins in different

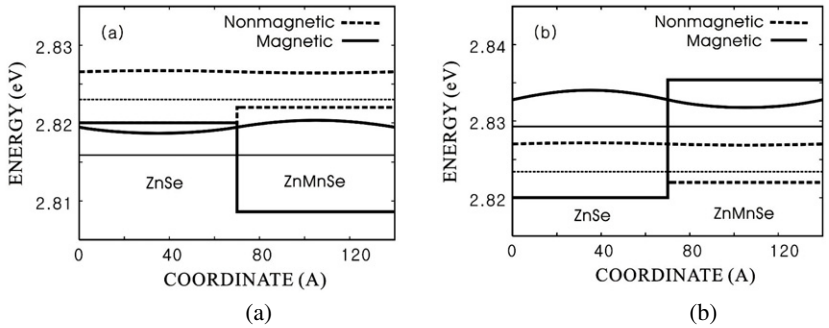

(a) (b)

Figure 3. The conduction bandedge profile without (dotted lines) and with (solid lines) Mn spin alignment in a magnetic field of 5 T for (a) the spin-down and (b) for the spin-up electron in a ZnMn/ZnMnSe superlattice is shown. The corresponding wavefunctions are shown in the 'spin–superlattice' formed in the structure.

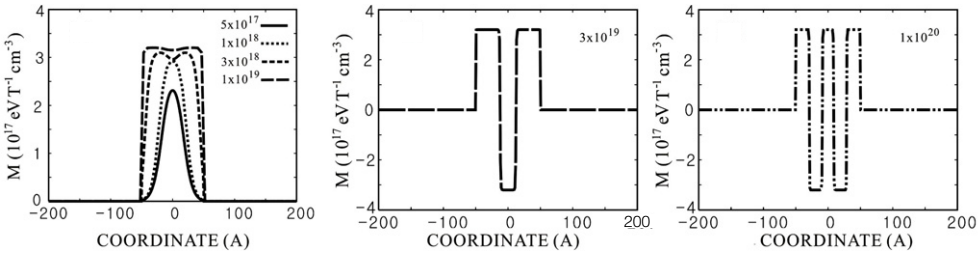

Figure 4. The magnetization due to Mn spin alignment in a 100 A GaMnAs quantum well is shown. In (a), the alteration of magnetization with increasing hole concentrations from 5×10^{17} cm^{-3}–10^{19} cm^{-3} is shown. With further increases in hole concentration, (b) and (c), the magnetization oscillates in orientation across the quantum well. This is due to the occupied energy levels and the corresponding wavefunctions for holes in the self-consistent potential (after [24]).

layers in specially designed DMS superlattices. This is an example of magnetically tuned wavefunction engineering.

Figure 4 shows the spontaneous magnetization of Mn ions in a 100 A $Ga_{0.95}Mn_{0.05}As/Al_{0.35}Ga_{0.65}As$ quantum well as a function of hole concentration, which can vary independently of the Mn concentration. Since the exchange interaction between Mn ions and itinerant holes increases with hole concentration, the magnetization increases with hole concentration, and saturates with a carrier density at about 3×10^{19} cm^{-3}. The shape of the magnetization is a reflection of the difference between spin-up and spin-down hole densities. As the hole concentration increases, higher subbands are occupied, and the shape of magnetization changes as the relative distribution of spin-up and spin-down holes changes. These Schrödinger–Poisson–DMS self-consistent calculations were performed in the valence four-band Luttinger model using the FEM, and illustrate the power of the method in successfully accounting for such large carrier concentrations [24].

We now consider an example of wavefunction engineering in a 100 A wurtzite GaN/AlGaN quantum well. When the structure is grown along the *c*-axis the resulting polarization leads to a distortion of the quantum well profile due to the large internal piezoelectric polarization fields. The wavefunctions are then displaced in position and the wavefunction overlap between electrons and holes is substantially reduced, as shown in figure 5(a). When the growth is

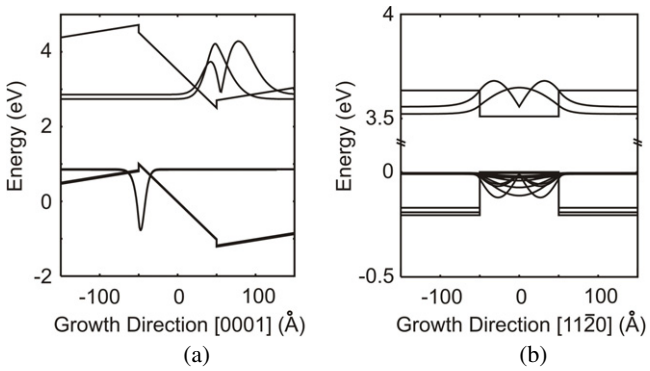

Figure 5. The remarkably high internal piezoelectric fields in wurtzite GaN/AlGaN structures distort the band-edge potential in quantum wells, as shown in (a), leading to a poor overlap of carrier wavefunctions. When grown along the [11$\bar{2}$0] direction the piezoelectric fields are along the plane, leading to better characteristics for quantum well lasers. Strain, piezoelectric effects, and inversion asymmetry effects have been included in the calculations (after [19]. Figure reproduced with permission from Elsevier).

along the [11$\bar{2}$0] direction, the spontaneous and piezoelectric polarizations are directed in the plane (still along the c-axis, which is in the plane). The quantum well potential is no longer distorted by the internal electric field and the wavefunction overlap is then 'engineered' to be large. The calculation of the energy levels and wavefunctions proceeds by employing a rotated Lagrangian with the new z'-axis directed towards the corresponding growth direction. The coordinate transformation $\mathbf{x}' = \mathbf{R}\mathbf{x}$ leads to the new rotated Lagrangian given by

$$\mathbf{L}_{\{x',y',z'\}}(\mathbf{k}') = \mathbf{R}\mathbf{L}_{\{x,y,z\}}(\mathbf{R}^{-1}\mathbf{k}')\mathbf{R}^{-1}. \tag{25}$$

The matrix elements of the transformed Lagrangian in the envelope function basis are separated, using symbolic algebra software, into terms involving powers of $k'_z = -\mathrm{i}\partial/\partial z'$ corresponding to the new growth direction. The rotated Lagrangian is then used in the finite element calculations [18]. A discussion of the rotation of the $\mathbf{k}\cdot\mathbf{P}$ Hamiltonian was given earlier in [11, 28, 29, 21]. This feature of the absence of bandedge profile distortion for the [11$\bar{2}$0] growth direction in GaN/AlGaN quantum wells has been investigated experimentally by [30, 31].

As a final example, we consider the design of an intersubband quantum cascade laser (QCL) structure for emitting in the terahertz (THz) region of the spectrum. Lasers in this region of the spectrum have special problems to overcome. The electronic transitions for photon emission are in the energy range 5–20 meV, so that the system has to be cooled to cryogenic temperatures, and the laser cavity has to be of the order of several hundred microns. In designing a quantum cascade laser, the goal of the optimization is to have a three-level system in which the carriers undergo a transition from energy E_3 to E_2, emitting a photon. The electrons are then depleted from E_2 by a transition from E_2 to E_1 on emitting interface and layer-confined longitudinal-optic phonons. The carriers then tunnel into the next period of the cascade, arriving in the uppermost level 3 of the next stage. Recently, the operation of THz lasers has been successfully demonstrated [32–34]. Here we are concerned with the optimized design of a single period of the cascade laser.

In order to design such a structure we consider a single period of a five-quantum well structure with the requirements that under an externally applied bias of say 2.5 kV cm^{-1} the energy differences are 16 meV ($\sim$77 μm or $\sim$3.9 THz) for the photonic transition, and $\sim$38 meV for the phonon emission. The calculation proceeds by coupling the one-band

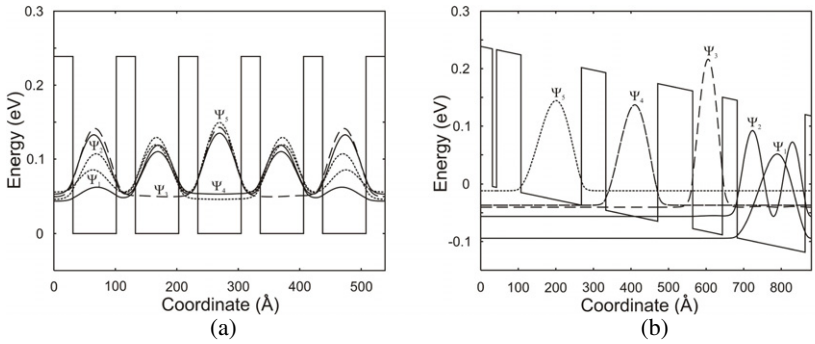

Figure 6. A five-well structure, representing one period of a QCL with energy level structure for emitting photons with energy 16 meV (3.9 THz) is shown before layer thickness optimization in (a). In (b) the structure after GA optimization is shown with well and barrier widths adjusted to obtain the energy levels under bias that are mentioned in the text.

finite element calculations of the energy levels of the nine-layer period to a Powell or genetic algorithm (GA) optimizer [35]. In figure 6(a) we show the initial well widths and energy levels with no bias. Initially, the well and barrier widths are uniformly the same for each well, and the wavefunctions have been shifted by the eigenvalues for purposes of this display. This may be compared with the final structure, figure 6(b), obtained through GA optimization for the well and barrier widths in order to obtain the desired energy level structure in $GaAs/Al_{0.3}Ga_{0.7}As$. The wavefunctions have been shifted vertically to have their x-axes coincide with the energy levels for display purposes. The gain in the QCL structure per period was not optimized with respect to the rate equations, and this work is as yet preliminary [36, 37] in this regard.

We note that the use of LO-phonon emission for depleting the carriers from E_2 to E_1 can also be optimized through the use of interface phonon modes and requiring that $(E_2 - E_1)$ lies in the set of interface mode energies. The interface modes extend over the entire structure and hence provide better overlap with the carriers. In this sense, we are employing phonon wavefunction engineering in the operation of the QCL [37].

5. Comparison with other methods

We have focused mainly on the $\mathbf{k} \cdot \mathbf{P}$ model and the use of the envelope function modelling for the electronic band structure near the centre of the Brillouin zone (BZ). Here we comment on the other alternatives for evaluating the electronic states in layered heterostructures so as to put their merits in perspective.

(a) In the *empirical tight binding model* (ETBM), originally put forward by Slater and Koster [38], the electronic states are considered to be linear combinations of atomic (s, p, d, ...) orbitals. The Hamiltonian's matrix elements between the atomic orbital states are not evaluated directly, but are instead introduced as free parameters to be determined by fitting the band gaps and band curvatures (effective masses) at critical points in the BZ. Depending on the number of orbitals and nearest neighbours used to represent the states, the ETBM requires that the overlap integrals be determined in terms of the measured direct and indirect band gaps and/or effective masses in the bulk material [39]. For example, the sp^3s^* basis with the second-nearest-neighbour scheme turns out to have 27 parameters for the zinc blende lattice structure, and the energies and effective masses are obtained from the diagonalization of the Hamiltonian. It has been emphasized by Lew Yan Voon

and Ram-Mohan [40] that the bulk band curvatures must be reproduced well in order to extend the analysis reliably to heterostructures since the effective masses play a crucial role in determining the energy levels in quantum wells, for example. Thus, reproducing the bulk bandgaps alone is not sufficient. The bulk energy bands are nonlinear functions of the ETBM parameters, which can be fitted by trial and error or by using optimization methods, such as genetic algorithms [41].

The lack of a direct relationship between the input parameters and the experimentally determined quantities is probably the single greatest disadvantage of the tight-binding method in making complicated band structure calculations. The strategy for employing the ETBM for heterostructures is analogous to the FEM in that we overlay atomic coupling matrices (the sub-Hamiltonians) in order to produce a global matrix for the heterostructure. The ETBM has been applied to superlattice band structure calculations [42]. A superperiodicity boundary condition is imposed on the global matrix, and the interface boundary conditions correspond to interpolated overlap integral parameters. It was originally thought that the momentum matrix elements for optical transitions require a refitting of the parameters for these matrix elements as well; however, it was shown by Lew Yan Voon and Ram-Mohan that one can obtain the optical matrix elements by invoking the Feynman–Hellmann theorem. We can relate the optical momentum matrix element to the derivative of the ETBM Hamiltonian with respect to the wavevector so that the same set of parameters that define the Hamiltonian can be reused in evaluating the optical matrix elements in a self-consistent manner [40]. The ETBM provides contributions from the entire BZ to the heterostructure energy levels, whereas the $\mathbf{k} \cdot \mathbf{P}$ method includes contributions only near the centre of the BZ. The computational requirements for 2D and 3D modelling within the ETBM would be more demanding in our opinion than the envelope function approach with FEM. Inclusion of electric and magnetic field effects are also much more complex in the ETBM than in the procedure we have reviewed in this article.

(b) While the inclusion of additional bands and overlaps of higher orbitals is a possible approach to improving the tight-binding modelling of energy bands in bulk semiconductors, the *effective bond orbital model* (EBOM) [43] uses spin-doubled s, p_x, p_y, p_z orbitals to generate an 8×8 Hamiltonian. A crucial difference between the EBOM and related tight-binding formulations is that the s and p orbitals are centred on the face-centred cubic lattice sites of the zinc blende crystal rather than on both of the two real atoms per lattice site. The resulting somewhat ad hoc formulation offers considerable computational savings in comparison with the ETBM. However, the main significance of the EBOM approach derives from the fact that the resulting secular matrix has a small-$\mathbf{k}$ expansion that exactly reproduces the form of the eight-band $\mathbf{k} \cdot \mathbf{P}$ Hamiltonian. This allows the EBOM input parameters to be readily expressed in terms of the experimentally measured parameters, such as the band gap, the split-off gap, and the zone-centre mass of each band, which has not been accomplished using the more involved ETBM. In fact, the EBOM can be thought of as an extension of the $\mathbf{k} \cdot \mathbf{P}$ method to provide an approximate representation of the energy bands over the full BZ. Since short-period superlattice bands sample wavevectors throughout the BZ, we may expect the EBOM to be more accurate than the $\mathbf{k} \cdot \mathbf{P}$ model for thin-layer structures. However, the EBOM is considerably less efficient computationally than the $\mathbf{k} \cdot \mathbf{P}$ method, especially for thicker superlattices. Each lattice position must be represented in the supercell technique, i.e., no envelope function approximation is made.

(c) The influence of core electrons in keeping the valence electrons outside of the core may be represented by an effective repulsive potential in the core region. When this is added to the

attractive ionic potential, the net 'pseudopotential' nearly cancels at short distances [44]. The valence states are orthogonal to the core states, and the resulting band structure theory corresponds to the nearly free-electron model. In the *empirical pseudopotential model*, the crystal potential is represented by a linear superposition of atomic potentials, which are modified to obtain good fits to the experimental direct and indirect band gaps and effective masses. Further details are presented by Cohen and Chelikowsky [45] and in the reviews by Heine and Cohen [46]. *Ab initio* approaches employ calculated band parameters (from the density-functional theory) in lieu of experimental data. Combinations of *ab initio* and empirical methods have been developed to a high level of sophistication [47]. Extension of the pseudopotential method to heterostructures entails the construction of a supercell to assure the proper periodic boundary conditions. With atomic potentials as the essential input, the electronic properties of the heterostructure can be determined, although the required computational effort far exceeds the demands of the $\mathbf{k} \cdot \mathbf{P}$ method. The relative merits of the $\mathbf{k} \cdot \mathbf{P}$ and pseudopotential approaches have been assessed [48]. Again, the inclusion of states from the entire BZ in the construction of heterostructure quantum states in these schemes entails heavy computational resources.

6. Concluding remarks

We have shown that the principle of least action can be employed to advantage in the modelling of semiconductor heterostructures by the FEM. This provides a natural way of including complex boundary conditions into the simulation. The FEM is not a low-accuracy method, but rather it can be used to solve quantum mechanical problems with double precision accuracy at the nanoscale. This modelling approach, implemented by us over the past two decades, now allows us to explore optoelectronic properties of complex heterostructures through numerical simulations [4, 49]. The wavefunction overlap, optical matrix elements, strain-induced band splittings leading to wavefunction mixing, energy level and wavefunction manipulation through modulation doping, use of magnetic impurity layers to alter distribution of the wavefunctions, and the application of external perturbations such as electric or magnetic fields are all increasingly of interest in controlling the actual shape of the wavefunctions. These represent aspects of wavefunction engineering. The properties of the structure can now be simulated and optimized on the computer before a heterostructure is actually grown [12, 26]. The fundamental shift in paradigm represented by wavefunction engineering is leading to the exploration of new electronic mechanisms and concepts, the exploration of basic physics, and a rapid turn-around in the design–growth–characterization cycle for developing new optoelectronic devices with 2D (quantum wire) and 3D (quantum dot) confinement of carriers. We are just beginning to explore the freedom in what may be called heterostructure architecture, in the design of new optoelectronic devices in three dimensions through this combination of fundamental theory and FEM computations. Such an approach is indispensable and perhaps inevitable for modelling nanoscale systems.

Acknowledgments

This work has been supported by the Air Force Office of Scientific Research under Grant F49620-03-1-0399. We want to thank John Albrecht, Alexi Girgis, William Goodhue, Jerry Meyer, Anusha Pokhriyal and Igor Vurgaftman for many discussions on topics presented here. We wish to thank Quantum Semiconductor Algorithms, Inc., for the use of their finite element and sparse matrix analysis software. KHY wishes to acknowledge the support of Kyung Hee

University during his sabbatical leave of absence in 2006 while portions of this work were completed.

References

[1] Bastard G 1988 *Wave Mechanics Applied to Semiconductor Heterostructures* (Les Ulis: Les Editions de Physique)

[2] Capasso F 1983 *J. Vac. Sci. Technol.* B **1** 457
Capasso F 1984 *Surf. Sci.* **142** 513

[3] Ram-Mohan L R 2002 *Finite Element and Boundary Element Applications to Quantum Mechanics* (Oxford: Oxford University Press)

[4] Ram-Mohan L R and Meyer J R 1995 *J. Nonlinear Opt. Phys. Mater.* **4** 191
Ram-Mohan L R, Dossa D, Vurgaftman I and Meyer J R 1999 *Handbook of Nanostructured Materials and Nanotechnology* vol 2, ed H S Nalwa (New York: Academic) chapter 15

[5] Zienkiewicz O C 1989 *The Finite Element Method* (New York: McGraw-Hill)
Zienkiewicz O C and Taylor R L 1994 *The Finite Element Method* (New York: McGraw-Hill)
Bathe K-J 1982 *Finite Element Procedures in Engineering Analysis* (Englewood Cliffs, NJ: Prentice-Hall)
Hughes T J R 1987 *The Finite Element Method* (Englewood Cliffs, NJ: Prentice-Hall)

[6] Gell-Mann M and Levy M 1960 *Nuovo Cimento* **16** 53

[7] Ram-Mohan L R, Moussa J and Yoo K H 2004 *J. Appl. Phys.* **95** 3081

[8] Vurgaftman I, Meyer J R and Ram-Mohan L R 1998 *J. Quant. Electron.* **34** 147

[9] Kane E O 1958 *J. Phys. Chem. Solids* **6** 236
Kane E O 1966 *Semiconductors and Semimetals* vol 1, ed R K Willardson and A C Beer (New York: Academic)
Kane E O 1982 *Handbook on Semiconductors* vol 1, ed W Paul (Amsterdam: North-Holland) p 193
Luttinger J M and Kohn W 1955 *Phys. Rev.* **97** 869

[10] Lowdin P O 1951 *J. Chem. Phys.* **19** 1396

[11] Weiler M H 1981 *Semiconductors and Semimetals* vol 16, ed R K Willardson and A C Beer (New York: Academic) p 119

[12] Pidgeon C R and Brown R N 1966 *Phys. Rev.* **146** 575

[13] Foreman B A 1993 *Phys. Rev.* B **48** 4964
Burt M G 1987 *Semicond. Sci. Technol.* **2** 460
Burt M G 1987 *Semicond. Sci. Technol.* **2** 701
Burt M G 1992 *J. Phys.: Condens. Matter* **4** 6651

[14] Luttinger J M 1956 *Phys. Rev.* **102** 1030

[15] van Dalen R and Stavrinou P N 1997 *Phys. Rev.* B **55** 15456

[16] Ram-Mohan L R, Vurgaftman I and Meyer J R 1999 *Microelectron. J.* **30** 1031
Ram-Mohan L R 2005 *Proc. 31st Int. Symp. on Compound Semiconductors (Seoul, Korea, Sept. 2004)* (*Institute of Physics Conference Series* vol 184) ed J-C Woo, H Hasegawa, Y-S Kwon, T Yao and K-H Yoo (Bristol: Institute of Physics Publishing) pp 1–8

[17] Lew Yan Voon L C, Willatzen M, Cardona M and Christensen N E 1996 *Phys. Rev.* B **53** 10703

[18] Bir G L and Pikus G E 1974 *Symmetry and Strain Induced Effects in Semiconductors* (New York: Wiley)
Pikus G E 1961 *Zh. Eksp. Teor. Fiz.* **41** 1258
Pikus G E 1962 *Sov. Phys.—JETP* **14** 898 (Engl. Transl.)
Sirenko Yu M, Jeon J B, Kim K W, Littlejohn M A and Stroscio M A 1996 *Phys. Rev.* B **53** 1997

[19] Ram-Mohan L R, Girgis A M, Albrecht J D, Litton C W and Steiner T D 2005 *27th Int. Conf. on the Physics of Semiconductors* ed J Menendez and C G Van de Walle (Melville, NY: American Institute of Physics) pp 941–2
Ram-Mohan L R, Girgis A M, Albrecht J D and Litton C W 2006 *Superlatt. Microstruct.* **39** 455–77

[20] Chuang S L and Chang C S 1996 *Appl. Phys. Lett.* **68** 1657
Chuang S L and Chang C S 1996 *Phys. Rev.* B **54** 2491

[21] Mireles F and Ulloa S E 1999 *Phys. Rev.* B **60** 13659
Mireles F and Ulloa S E 2000 *Phys. Rev.* B **62** 2562

[22] Ren G B, Liu Y M and Blood P 1999 *Appl. Phys. Lett.* **74** 1117

[23] Dugdale D J, Brand S and Abram R A 2000 *Phys. Rev.* B **61** 12933

[24] Jang S T, Yoo K H and Ram-Mohan L R 2006 *Proc. 13th Int. Symp. on Physics of Semiconductors and Applications* at press

[25] For a recent compilation of band parameters, see Vurgaftman I, Meyer J R and Ram-Mohan L R 2001 *J. Appl. Phys.* **89** 5815

Vurgaftman I and Meyer J R 2003 *J. Appl. Phys.* **94** 3675
[26] Meyer J R, Vurgaftman I, Yang R Q and Ram-Mohan L R 1996 *Electron. Lett.* **32** 45
Vurgaftman I, Meyer J R and Ram-Mohan L R 1997 *Photon. Technol. Lett.* **9** 170–2
[27] Dai N, Luo H, Zhang F C, Samarth N, Dobrowolska M and Furdyna J K 1991 *Phys. Rev. Lett.* **67** 3824
Dai N, Ram-Mohan L R, Luo H, Yang G L, Zhang F C, Dobrowolska M and Furdyna J K 1994 *Phys. Rev.* B **50** 18153
[28] Hoffman C A, Meyer J R, Wagner R J, Bartoli F J, Chu X, Faurie J P, Ram-Mohan L R and Xie H 1990 *J. Vac. Sci. Technol.* A **8** 1200–5
[29] Yoo K H 1990 Magneto-optical studies of HgTe/CdTe superlattices with bandgaps in the infrared *PhD Thesis* MIT
[30] Ng H M 2002 *Appl. Phys. Lett.* **80** 4369
Bykhovski A, Gelmont B and Shur M 1993 *Appl. Phys. Lett.* **63** 2243
[31] Ghosh S, Brandt O, Grahn H T and Ploog K H 2002 *Phys. Status Solidi* b **234** 882
[32] Kumar S, Williams B S and Qing Hu 2006 *Appl. Phys. Lett.* **88** 12123
[33] Fasching G, Benz A, Zobl R, Andrews A M, Roch T, Schrenk W, Strasser G, Tamosiunas V and Unterrainer K 2006 *Physica* E **32** 316
[34] Worral C, Alton J, Houghton M, Barbieri S, Beere H E, Ritchie D and Sirtori C 2006 *Opt. Express* **14** 171
[35] Press W H, Teukolsky S A, Vetterling W T and Flannery B R 1992 *Numerical Recipes* (Cambridge: Cambridge University Press)
[36] Ram-Mohan L R, Girgis A, Pokhriyal A and Goodhue W 2006 unpublished results
[37] Menon V M, Goodhue W D, Karakashian A S and Ram-Mohan L R 2000 *J. Appl. Phys.* **88** 5262–7
Menon V M, Ram-Mohan L R, Goodhue W D, Karakashian A S, Naweed A, Gatesman A and Waldman J 2002 *Physica* E **15** 197–201
Menon V M, Ram-Mohan L R, Goodhue W D, Gatesman A J and Karakashian A S 2002 *Physica* B **316/317** 212–5
Menon V M, Goodhue W D, Karakashian A S, Naweed A, Plant J, Ram-Mohan L R, Gatesman A, Badami V and Waldman J 2002 *Appl. Phys. Lett.* **80** 2454–6
[38] Slater J C and Koster G F 1954 *Phys. Rev.* **94** 1498
[39] Chadi D J and Cohen M L 1975 *Phys. Status Solidi* b **68** 405
Vogl P, Hjalmarson H P and Dow J D 1983 *J. Phys. Chem. Solids* **44** 365
[40] Lew Yan Voon L C and Ram-Mohan L R 1993 *Phys. Rev.* B **47** 15500–8
[41] Klimeck G, Bowen R C, Boykin T B and Cwik T A 2000 *Superlatt. Microstruct.* **27** 519
[42] Smith D L and Mailhiot C 1990 *Rev. Mod. Phys.* **62** 173
Schulman J N and Chang Y-C 1985 *Phys. Rev.* B **31** 2056
Schulman J N and Chang Y-C 1986 *Phys. Rev.* B **33** 2594
Lew Yan Voon L C and Ram-Mohan L R 1994 *Phys. Rev.* B **50** 14421
[43] Chang Y C 1988 *Phys. Rev.* B **37** 8215
Loehr J P 1994 *Phys. Rev.* B **50** 5429
Loehr J P 1997 *Physics of Strained Quantum Well Lasers* (New York: Kluwer–Academic)
[44] Phillips J C and Kleinman L 1959 *Phys. Rev.* **116** 287
Cohen M H and Heine V 1961 *Phys. Rev.* **122** 1821
[45] Cohen M L and Chelikowsky J R 1988 *Electronic Structure and Optical Properties of Semiconductors* (*Springer Series in Solid-State Sciences* vol 75) ed M Cardona (Berlin: Springer)
[46] Heine V 1970 *The Pseudopotential Concept* (*Solid State Physics* vol 24) ed H Ehrenreich, F Seitz and D Turnbull (New York: Academic) p 1
Cohen M L and Heine V 1970 *The Fitting of Pseudopotentials to Experimental Data and their Subsequent Application* (*Solid State Physics* vol 24) ed H Ehrenreich, F Seitz and D Turnbull (New York: Academic) p 38
[47] Wang L-W and Zunger A 1996 *Semiconductor Nanoclusters* (*Studies in Surface Science and Catalysis* vol 103) ed P V Kamat and D Meisel (New York: Elsevier Science) p 161
[48] Wood D M and Zunger A 1996 *Phys. Rev.* B **53** 7949
Wang L-W, Wei S-H, Mattila T, Zunger A, Vurgaftman I and Meyer J R 1999 *Phys. Rev.* B **60** 5590
[49] Meyer J R, Hoffman C A, Bartoli F J and Ram-Mohan L R 1966 *Novel Optical Materials and Applications* ed I C Khoo, F Simone and C Umeton (New York: Wiley) pp 205–37